Analytica Chimica Acta 1135 (2020) 29–37

Contents lists available at ScienceDirect

Analytica Chimica Acta

journal homepage: www.elsevier.com/locate/aca

An ultrasensitive non-noble metal colorimetric assay using starch-iodide complexation for Ochratoxin A detection

Akkapol Suea-Ngam , Leif-Thore Deck , Philip D. Howes *, Andrew J. deMello *

Institute for Chemical and Bioengineering, Department of Chemistry and Applied Biosciences, ETH Zürich, 8093, Zürich, Switzerland

HIGHLIGHTS

- Novel colorimetric antibody-aptamer sandwich assay using starch-iodine complexation.
- Central composite design for fast and efficient sensor optimization.
- Ultrasensitive detection of OTA using PADs with LoD of 20 pg mL^{-1} using 5 μL.
- Applied for OTA detection in beverages, urine and human serum.

GRAPHICAL ABSTRACT

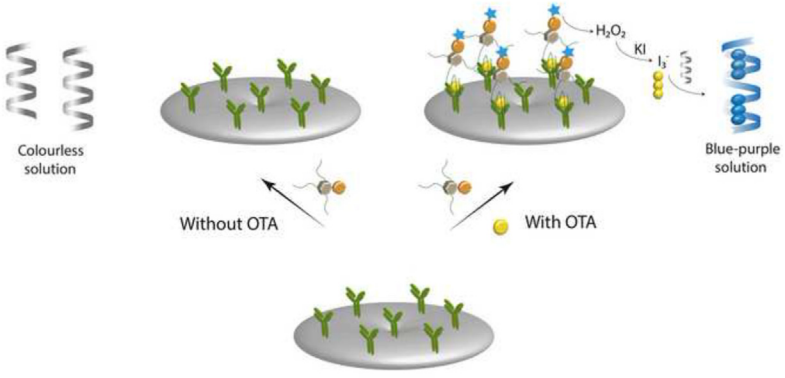

ARTICLE INFO

Article history:
Received 25 June 2020
Received in revised form
24 July 2020
Accepted 15 August 2020
Available online 20 August 2020

Keywords:
Paper-based analytical device
Antibody-aptamer
Colorimetric
Mycotoxin
Starch-iodine complex
Point-of-care

ABSTRACT

Colorimetric sandwich-type biosensors that can both provide sensitivity competitive with fluorescence-based approaches, and leverage reagents that are cost-effective, widely available and as safe as possible, are highly sought after. Herein, we demonstrate an alternative highly-sensitive colorimetric method for paper-based sandwich-type biosensing that uses starch−iodide complexation to simplify practical biosensing using ubiquitous reagents. Targeting the mycotoxin ochratoxin A (OTA), a covalently-immobilised OTA antibody on a cellulose surface captures OTA and forms a sandwich with OTA aptamer-conjugated glucose oxidase. Adding the chromogenic reagents at an optimized concentration, a distinct blue color develops within 30 min, offering excellent contrast with the clear/white of the negative sample. With a sampling volume down to just 5 μL, the assay exhibits concentration limits of detection and quantitation of 20 and 320 pg mL^{-1}, respectively, and a linear range from 10^{-1} to 10^5 ng mL^{-1} ($R^2 = 0.997$). The method displays excellent selectivity against related mycotoxins, excellent %recovery (95−117%) and robust operation in complex matrices (beer, urine and human serum), with no significant difference *versus* gold-standard liquid chromatography. Along with its excellent analytical performance, this assay benefits from non-toxic and extremely cheap reagents that can be safely disposed of in the field, and presents an attractive alternative to toxic dyes and nanoparticles.

1. Introduction

Simple and robust routes for colorimetric detection at low

* Corresponding authors.
E-mail addresses: philip.howes@chem.ethz.ch (P.D. Howes), andrew.demello@chem.ethz.ch (A.J. deMello).

https://doi.org/10.1016/j.aca.2020.08.028
0003-2670/

analyte concentrations have been sought after for centuries [1–3]. In more recent times, such approaches have been translated to paper-based analytical devices (PADs), providing simple solutions for point-of-need and point-of-use testing [4–6]. Although colorimetric detection schemes are typically less sensitive than electrochemical- or fluorescence-based methods [7], they are ideally suited for application in PADs due to the simplicity of both readout and operation [8,9].

Colorimetric detection methods have traditionally used ligands that form complexes with a specific target ion or molecule (e.g. the complexation of Ni with dimethylglyoxime [10]), or covalent bond-forming reactions (e.g. creatinine with picrate [2]). However, such approaches are highly specific to their target analyte, and are thus inherently limited in their versatility and scope. More recently, noble metal nanoparticles have been extensively investigated and employed as reporters in colorimetric sensing [11]. Their intense localized surface plasmon resonance (LSPR) leads to phenomena that can readily be harnessed in biosensing [12,13]. However, there is an inherent cost associated with the use of gold, silver and platinum (even at low masses or concentrations) that limits how far device costs can be driven down [14]. In addition, the synthesis of noble metal nanoparticles remains a non-trivial and resource-intensive undertaking [15]. Finally, and critically, there are ongoing concerns related to the environmental effects of metal nanoparticles, with little understanding of how composition, size, shape and surface functionality affect their downstream toxicity [16]. Such disadvantages have inspired us to investigate viable alternatives that circumvent such issues, yet retain the required simplicity and sensitivity.

Various biosensor platforms have used the enzyme by-product H_2O_2 to oxidize indicating dyes (e.g. 3,3′,5,5′-Tetramethylbenzidine, TMB, and 2,2′-azino-di-(3-ethylbenzthiazoline sulfonic acid), ABTS™) [17,18], however such dyes are relatively expensive, offer low sensitivity, and are not environmentally friendly. Using the same oxidizing strategy, but with the cheap and environmentally benign reagents iodine and potassium iodide (KI), an extremely effective colorimetric signal can be developed. Here, dissolution of elemental iodine in aqueous KI yields triiodide (I_3^-), which can subsequently form intermolecular charge-transfer complexes and polyiodide homopolymers with starch molecules, yielding a dark blue/purple coloration [19]. Although this intense chromogenic response has commonly been used for direct starch testing in food [20], few works have investigated the phenomenon as a novel concept in the medical diagnostics field, despite the obvious potential [21]. For example, an important work by Liu et al. demonstrated the use of starch–iodide complexation to generate a colorimetric response in a microwell plate-based assay for the detection of prostate specific antigen (PSA), showing detection down to 0.46 pg mL^{-1} [22]. However, although this approach would be suitable for clinical and laboratory settings, it is not deployable to the point-of-care or resource-limited settings. The idea has been recently extended to a PAD system to detect hydrogen peroxide and glucose (with LODs of 0.05 and 0.1 mM respectively) [23], however the expansion and optimization of this approach into sandwich assays for field-deployable and point-of-care platforms for diagnostics has not been demonstrated previously. In summary, we feel there is much potential still to be unlocked in the application of this phenomenon for universal and point-of-care diagnostics, which inspired us to extend the technique into a PAD system incorporating a sandwich-type analyte capture mechanism, for a new class of molecular target.

Herein, we report a simple yet powerful antibody–aptamer-based PAD with colorimetric readout targeting ochratoxin A (OTA), a carcinogen (class 2 B) generated by *Aspergillus* and *Penicillium* contaminated in food and drink and in bodily fluids, as a model toxin [24]. As illustrated in Scheme 1, covalent immobilization of *anti*-OTA antibodies (antiOTA) on a cellulose surface (Scheme S1) allows capture of OTA and further labelling by aptamer-conjugated glucose oxidase (AGOx) *via* a sandwich mechanism. Subsequent introduction of a starch, KI and glucose solution into the PAD chamber yields a distinct color change to blue/purple for the positive test due to the H_2O_2 produced by AGOx. Smartphone-captured images can be directly analyzed to extract color intensity and quantify analyte levels. Due to high surface-to-volume ratio, this approach allows high sensitivity and precise quantitation of OTA in complex matrices, such as beer, urine, and human serum. Furthermore, through the use of experimental design, rapid and resource-efficient optimization of KI, starch and glucose concentrations was performed. The optimized PAD-based sensor demonstrates much promise for environmentally friendly, highly sensitive, cost-effective, simple and robust biosensing for deployment in a variety of low resource settings.

2. Materials and methods

2.1. Reagents and materials

Rabbit anti *Aspergillus ochraceus* ochratoxin A (antiOTA) was purchased from Bio-Rad (California, USA). The OTA aptamer (5′-biotin-AAA AAA AAA AGAT CGG GTG TGG GTG GCG TAA AGG GAG CAT CGG ACA-3′) was purchased from Microsynth (Balgach, Switzerland). Ochratoxin A (OTA), Aflatoxin B1 (AFB1), Aflatoxin B2 (AFB2), citric acid, sodium citrate, glucose, KI, starch, HEPES, EDTA, Trizma base™, Tween 20, $NaNO_3$, $CaCl_2$, PBS tablets, NaCl, skimmed milk, $NaIO_4$ and KCl were purchased from Sigma-Aldrich (Buchs, Switzerland) and used as received. All other reagents, including Ochratoxin B (OTB) (AdipoGen AG, Epalinges, Switzerland), HCl (Fluka, Buchs, Switzerland), 3-aminopropyltrimethoxysilane (Tokyo Chemical Industry, Eschborn, Germany), glucose oxidase-conjugated avidin (Rockland, Hamburg, Germany) and $MgCl_2$ (Acros Organics, Geel, Belgium), were analytical reagent grade and used as received. All aqueous solutions were prepared with DNase and RNase free water (Thermo Fisher Scientific, Reinach, Switzerland). All images were taken using an unmodified Sony Xperia XZ Premium smartphone camera and analyzed using ImageJ software (National Institutes of Health, Maryland, USA).

2.2. Device fabrication

Circular wax chambers of 8 mm diameter with 1 mm thickness were printed on Whatman No. 1 cellulose paper (Sigma-Aldrich, Buchs, Switzerland) prior to incubation at 170 °C on a heating plate for 1 min (to allow wax to penetrate into the paper). Yellow wax was chosen to define the sample reservoir, as it is the 'opposite' color—following the logic of typical color models—of our starch–iodide complex, which develops as blue/purple. Using yellow has the added benefit of reducing the potential for interference by the color of the sample, which in the current study was also yellow (beer, human serum and urine). An antibody conjugation protocol reported by Peng et al., employing the amino-aldehyde reaction to form imine linkages, was used (Scheme S1) [25]. Addition of amino groups onto the cellulose was achieved by applying a mixture of 3-aminopropyltrimethoxysilane (APS) and acetone (1:10) to the chambers, before drying at room temperature for 5 h. Subsequently, the PAD was rinsed with acetone and baked in an oven at 110 °C for 3 h to complete silicon-oxygen condensation on the cellulose surface. Next, antiOTA antibodies were treated with $NaIO_4$ in acetate buffer (pH 5.5) to generate aldehyde groups at the end of the Fc-region, and then introduced into the amino functionalized chamber, forming imine linkages between the

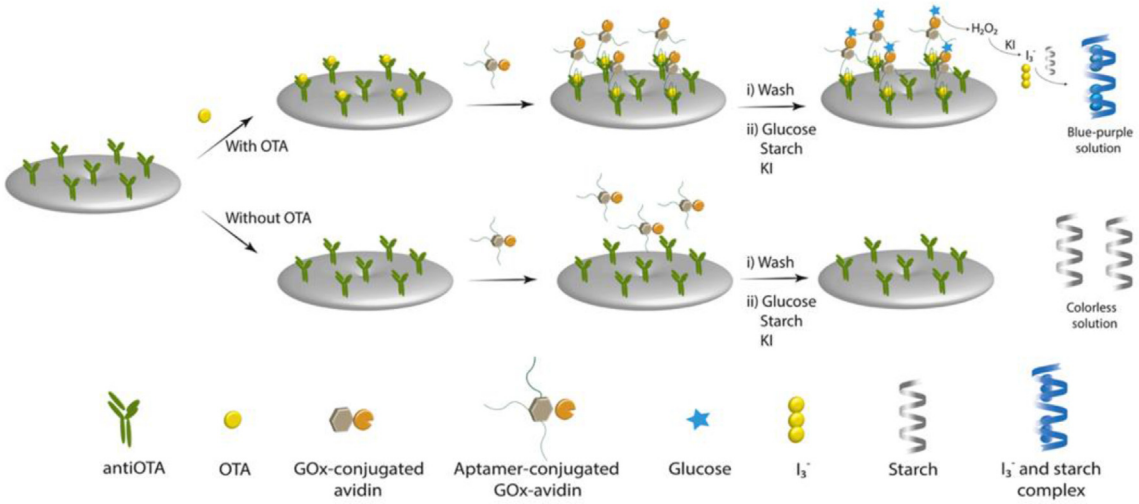

Scheme 1. A schematic illustration of the colorimetric paper-based assay. Surface-immobilized antiOTA antibodies bind OTA from solution, with aptamer-GOx conjugates then binding to OTA and forming a sandwich complex. Subsequent addition of glucose, starch and potassium iodide sees the GOx produce H_2O_2, leading to the formation of triiodide that complexes with starch and produces the blue color. In the absence of OTA, the sandwich complex cannot form and the blue coloration does not occur.

treated paper and antiOTA at room temperature, and over a period of 1 h. Finally, devices were rinsed three times with buffer containing 10% (w/v) skimmed milk powder, 50 mM Tris, 0.15 M NaCl and 0.05% Tween 20 (pH 7.4), allowed to dry at room temperature and then stored in the dark at 4 °C.

2.3. Aptasensor-GOx conjugation

Biotinylated aptamers (sequence previously reported in Ref. [26]) were conjugated with avidin-conjugated glucose oxidase, *via* biotin-avidin binding at a 3:1 M ratio (4 °C overnight). Solutions were stored in the dark at 4 °C, then diluted to 10 nM in binding buffer (10 mM Tris, pH 8.5, 120 mM NaCl, 5 mM KCl, 10 mM $MgCl_2$, and 20 mM $CaCl_2$) before use.

2.4. Assay procedures

For the UV–vis spectroscopy experiment, 10 μL of 1000 U L^{-1} AGOx/GOx, 10 μL of 100 μM H_2O_2, 100 μL of 10% starch solution, 50 μL of 5.2 mM KI, and 40 μL of 22.5 mM of glucose were used and adjusted to 1 mL using PBS buffer 100 mM pH 7.42, resulting in 10 U L^{-1} AGOx/GOx, 1 μM H_2O_2, 1% starch solution, 260 mM KI, and 900 μM of glucose.

For the GOx optimization experiments in microwells, 25 μL of 3.6 mM glucose and 25 μL of AGOx/GOx was added into each well, followed by 50 μL of 520 mM KI and 2% starch solution. Solutions were incubated for 30 min before capturing images with a smartphone for further analysis using the ImageJ software.

For GOx optimization on the PAD, 1 μL of GOx and 1 μL of glucose was added to each reservoir, followed by 3 μL of the CCD optimised iodine and starch solutions (4.5 mM glucose, 1.5% starch, 450 mM KI). The PAD was incubated in a humid chamber for 30 min to generate the color, before capturing images for analysis *via* ImageJ.

In experiments assessing the analytical performance, 5 μL of standard solution was applied to the antibody-immobilized reservoir, left for 10 min, then the samples were removed by micropipette, followed by three washes with 20 μL milliQ water to remove unbound sample. Then, 5 μL aptamer/GOx was applied to form the sandwich, before washing three times with milliQ water after 10 min, followed by 5 μL of the optimized chromogenic reagents (0.9 mM glucose, 1% starch and 260 mM KI) for a 30 min incubation in a humid chamber before capturing images for analysis.

2.5. System optimization

Central composite design (CCD), an experimental design method, was used to optimize concentrations of KI, glucose and starch. The levels and ranges of these (independent) variables are provided in Table 1 and Fig. S1. The three variables/factors were studied at three levels; therefore, the CCD model required 20 separate experiments, inclusive of 5 centre point repeats (Table 2 and S2). To allow possible application of PADs in a field, remote or point-of-care setting, negative (i.e. no analyte or H_2O_2) controls were used for background subtraction. Captured images were imported into the ImageJ software, where simple RBG analysis was performed. The signal color intensity was determined by subtracting the negative control as a background for each image. Thus, the response signals were normalized ($normalized\ intensity = \frac{Background\ intensity - Sample\ intensity}{Background\ intensity} \times 100$) before optimization. Response surface modelling, statistical analysis and optimization were performed using the matrix and equations described in previous studies [26,27]. Paired t-tests and coefficients of determination (R^2) were used to assess output data. Intensities were normalized using the percentage difference between the analyte and the background signal. Data operation was investigated using Equation S1 and S2. Response data from the experiments were expressed by polynomial regression, generating the following model,

Table 1
Experimental ranges and levels of the three independent variables used in the central composite design for signal optimization.

Variables (unit)	Actual Level			Coded Level		
	Low	Middle	High	Low	Middle	High
Starch (% w/v)	0.5	1	1.5	−1	0	1
KI (mM)	100	200	300	−1	0	1
Glucose (μM)	300	600	900	−1	0	1

Table 2
Experiments conducted for the central composite design for signal optimization using KI concentration, starch concentration and glucose concentration. The normalized intensity response data for the experiments and the back-calculated response from the resultant model are shown.

Run	Coded value			%Normalized intensity	
	KI	Starch	Glucose	Experiment	Predicted
1	1	1	1	63.32 ± 0.76	63.77
2	1	1	−1	29.78 ± 0.19	33.61
3	1	−1	1	60.38 ± 0.47	62.12
4	1	−1	−1	31.86 ± 0.05	29.31
5	−1	1	1	60.41 ± 0.12	59.24
6	−1	1	−1	31.62 ± 0.15	26.16
7	−1	−1	1	72.20 ± 0.31	64.65
8	−1	−1	−1	33.10 ± 0.35	28.93
9	1.68	0	0	50.05 ± 0.48	46.18
10	−1.68	0	0	32.92 ± 0.08	42.05
11	0	1.68	0	51.64 ± 0.33	51.25
12	0	−1.68	0	46.53 ± 0.21	52.19
13	0	0	1.68	68.56 ± 0.10	70.65
14	0	0	−1.68	12.14 ± 0.34	15.31
15	0	0	0	50.95 ± 0.17	51.00
16	0	0	0	51.37 ± 0.15	51.00
17	0	0	0	51.20 ± 0.20	51.00
18	0	0	0	51.59 ± 0.15	51.00
19	0	0	0	51.03 ± 0.17	51.00
20	0	0	0	50.80 ± 0.17	51.00

$$y = intercept + \sum_{i=1}^{n} b_i X_i + \sum_{i=1}^{n} b_{ii} X_i^2 + \sum_{i=1}^{n-1} \sum_{j=i+1}^{n} b_{ij} X_i X_j + \varepsilon \qquad (2)$$

where y is the predicted response, b_i is the linear coefficient, b_{ii} is the quadratic coefficient, b_{ij} is the interaction coefficient, with X_i and X_j representing the variables. Optimum variable values were predicted *via* response surface analysis of the combined variables. Constraints in this regard were applied to predict the optimum variable conditions that would yield the highest normalized signal intensity (Table 2). Model efficiency was assessed by performing the suggested experiments and comparing real and predicted results. Coefficients of determination and paired t-tests were then used to assess model robustness. The numerical optimization of the response was predicted according to a second order polynomial model.

2.6. Operation of PAD and real sample analysis

The PAD assay was performed by adding 5 μL of sample into the paper reservoir, leaving for 10 min, then removing the excess sample solution by micropipette. The wells were washed three times with 20 μL milliQ water to remove unbound sample. Next, 5 μL aptamer/GOx was applied to form the sandwich complex for 10 min, before washing with milliQ water three times. Finally, 5 μL of chromogenic reagents were added and incubated for 30 min in a humid chamber before taking images for analysis. Ultrahigh performance liquid chromatography (UPLC) was used to compare both standard OTA solutions and spiked-beer samples (following procedures reported by Wei et al. [28]) Beer samples were degassed with argon and then applied directly to either the PADs or UPLC for analysis. Testing was performed by spiking OTA into beer at 1, 5 and 10 ng mL^{-1}. For complex sample analysis, artificial urine and human serum (Sigma-Aldrich, Buchs, Switzerland) were assayed, comparing blank and OTA-spiked samples at the same concentration used for the beer samples.

2.7. Characterisation

Limits of detection (LOD) and limits of quantification (LOQ) were calculated as 3 and 10 times the standard deviation of the blank measurement, respectively. Values were calculated using a linear fit of the linear range in the plots of signal intensity versus log concentration.

3. Results and discussion

3.1. Colorimetric method validation

To confirm that starch–iodide complex formation is initiated by H_2O_2, a series of solutions containing permutations of 0.1 mM H_2O_2, 0.2 M KI and/or 1% (w/v) starch in PBS were probed using absorption spectroscopy. Starch solutions containing either KI or H_2O_2 exhibited minimal absorbance between 300 and 800 nm (Fig. 1a). In contrast, the H_2O_2 and KI solution was pale-yellow in color, with a distinct absorption peak between 290 and 360 nm, indicative of residual I_3^- formation [29]. With all three components present, the solution turned a distinct blue, with a broad absorption peak centered at 560 nm, and lower intensity I_3^- peaks still visible below 400 nm. The reduction and shift of the I_3^- peaks, and the emergence of the 560 nm peak, confirmed starch–iodide complexation [22], which only occurs when the I^- is oxidized by H_2O_2 into I_2 and recombined with I^- to form I_3^-.

Next, we investigated whether H_2O_2 generated by GOx would also initiate starch–iodide complexation, and whether AGOx, which is required to allow biotinylated aptamer and GOx conjugation *via* biotin-avidin interaction, showed the same efficacy as unconjugated GOx. Specifically, enzyme was introduced into a KI/

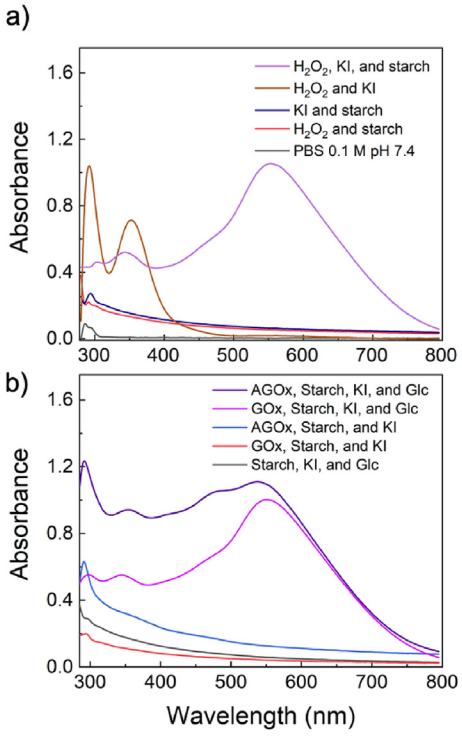

Fig. 1. Different permutations of the assay components were studied in solution by UV–vis absorption spectroscopy to characterize the starch–iodide complexation process. The plots present absorption spectra of (a) H_2O_2, starch and KI combinations, and (b) starch, KI tested with and without glucose (Glc), aptamer-conjugated GOx (AGOx) and unconjugated GOx. All solutions were prepared in 0.1 M PBS buffer at pH 7.4.

starch solution, with subsequent addition of glucose initiating the production of H_2O_2. Fig. 1b shows the development of absorption features indicative of starch–iodide complexation for both GOx and AGOx, with solutions turning blue/purple. Interestingly, in the presence of AGOx, an increase of the absorption band between 300 and 560 nm was observed, which indicates formation of amylopectin (an insoluble hyper-branched glucose polymer) [30], and suggests that avidin could form an amylopectin-like amylose complex. This observation is consistent with the results of Lui et al., who suggested that peptides or proteins enhance color intensity in starch–iodide complexes *via* the formation of films or particles [23]. Here, we believe that avidin, present in the AGOx conjugate, plays a similar role. Overall, the data confirm that the proposed AGOx-based H_2O_2-induced colorimetric signal transduction strategy is viable and of potential utility in a surface-based analyte sandwich format.

3.2. Assay optimization

Having established the basic working principle, we then determined which reagent concentrations (glucose, starch and potassium iodide) would yield optimal signal strength. In previous studies, assay optimization was performed *via* a one-factor-at-a-time (OFAT) approach to determine appropriate iodine, starch and H_2O_2 levels. In this respect, it is likely that application of a design of experiments (DoE) approach—such as central composite design (CCD), which utilizes simple matrix-based regression to predict optimal values [31]—would be useful in extending and optimizing the performance of the starch-iodide system towards a range of biosensing applications. Here, we used CCD to guide this process, as this model contains linear, quadratic, and interaction coefficients that allow capture of non-linear relationships between variables that are overlooked in the typical OFAT approach [31]. Table 1 and Fig. S1 presents the independent variables used in the optimization. The ranges were refined from literature results by performing a small number of initial test experiments, and then converted to coded values (which are used to normalize the values/ranges between variables such that resultant coefficients can be directly compared). CCD analysis was performed using a microwell plate-based assay as described in the Methods section (see Fig. S1), using the design model shown in Table 2 and S2. This yielded the polynomial equation

$$y = 51.0 + 1.23[KI] - 0.28[Starch] + 16.5[Glucose] - 2.43[KI]^2 + 0.25[Starch]^2 - 2.84[Glucose]^2 + 1.77[KI][Starch] - 0.73[KI][Glucose] - 0.66[Starch][Glucose] \quad (1)$$

which models the percentage difference between the analyte signal and the background intensity, given the coded values of the reaction variable concentrations. Fig. 2a–c shows three contour plots of normalized signal intensities as a function of two variables at a time. Fig. 2a and b indicate an optimal range for starch and KI concentrations between 0.5 and 1.5% (w/v) and 200–300 mM, respectively, with Fig. 2b and c indicating an increasing signal intensity with increasing glucose concentration. Optimal values for each variable were determined by partial differentiation of Equation (1), and yielded values of 258.8 mM for KI, 1.01% (w/v) for starch, and 902 μM for glucose. These estimates were rounded to 260 mM for KI, 1% (w/v) for starch, and 900 μM for glucose in subsequent experiments. Red circles in Fig. 2a–c indicate the as-calculated values, with optimized parameters providing 72% of the normalized intensity for the blue/purple starch–iodide complex in the presence of 0.1 U L^{-1} GOx, for 30 min. The predicted response values extracted from the model were then compared to experimental data (Table 2), with paired t-tests (t-value = 0.027 < t-critical = 2.09, α = 0.05, 95% confidence) indicating no significant difference between the experimental and predicted data sets (N = 20). Additionally, both experimental and predicted data exhibited excellent correspondence (R^2 = 0.934), as shown in Fig. 2d.

3.3. Enzymatic activity

After optimizing reagent concentrations, we next assessed the GOx activity. In our system, H_2O_2 is first produced by oxidation of glucose to glucono-1,5-lactone, and free I^- is then oxidized to I_3^-, which subsequently initiates starch–iodide complexation. A GOx concentration series between 0.1 and 10 U L^{-1} was prepared in solutions containing the optimized reagent concentrations in a microwell plate format. Fig. 3a shows the dose-dependent relationship between GOx and signal intensity, measured 30 min after GOx addition. This time was chosen based on a study of signal intensity over time, which showed the response to plateau after 30 min (Fig. S2). These data are extracted by image analysis of the microwell plate, showing a linear range between 0.1 and 1.0 U L^{-1} (R^2 = 0.989, Fig. 3a inset). The use of optimized reagent concentrations ensured high analytical sensitivity with respect to GOx detection, yielding an LOD of 0.03 U L^{-1} and a limit of quantitation (LOQ) of 0.10 U L^{-1}, based on 3 and 10 times the standard deviation of background, respectively.

Having determined the efficacy of the approach in free solution, we next sought to translate the sensing and signal transduction mechanisms to a PAD format. Antibody was modified onto the PAD covalently using a process as illustrated in Scheme S1. Fig. 3b presents data measured using the same conditions as in Fig. 3a, but with reactions proceeding in paper wells instead of microwells. The paper wells require a sample volume of just 5 μL, compared to 100 μL for the well plate, but still achieve an equivalent LOD (0.03 U L^{-1}) and LOQ (0.09 U L^{-1}), and wider linear range (0.1–6.0 U L^{-1}, R^2 = 0.987), compared to the well-based assay (Fig. 3b inset). The main factor in this excellent performance of the PAD-based measurements is the large surface-to-volume ratio—a key advantage in microfluidic systems [32,33]—resulting in a much larger effective sensing area versus the microwell surface assay. These preliminary data indicate that the proposed strategy is highly suitable for use within a PAD-based sensing format.

3.4. Analytical performance

Dynamic Range, Limit of Detection and Limit of Quantitation: To test the developed sensing system (illustrated in Scheme 1), a calibration curve was constructed using an OTA concentration series between 10^{-2} and 10^6 ng mL^{-1}. Using the optimized reagent concentrations, signals were extracted and quantified by image

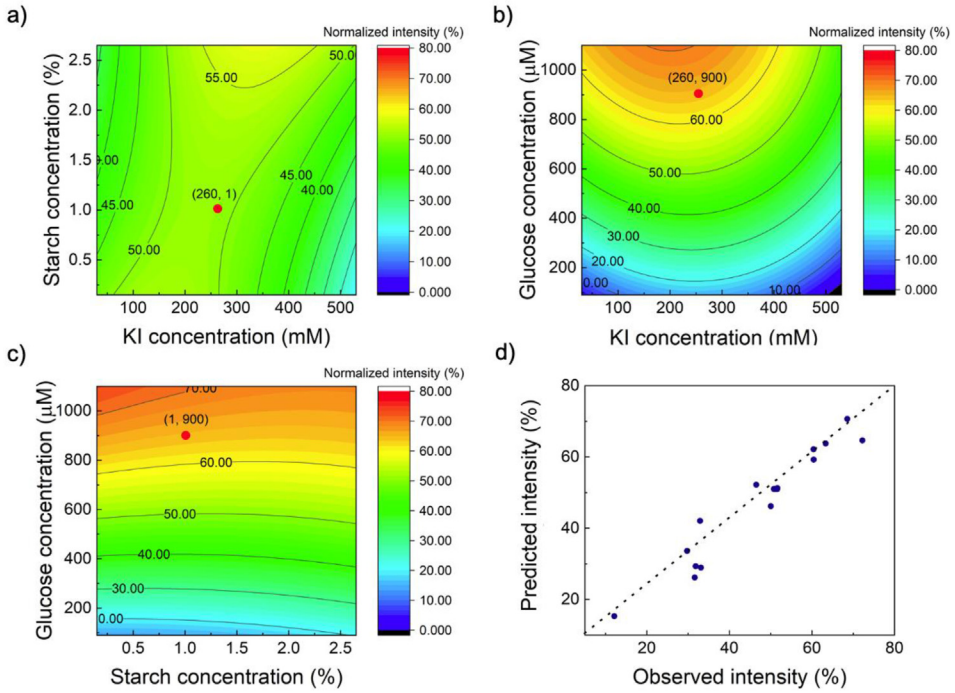

Fig. 2. Central composite design was used to ascertain the concentrations of three assay variables, starch concentration (%), glucose concentration (μM) and KI concentration (μM), that yielded optimal assay response. (a, b, c) Surface contour plots report how normalized signal intensities (assay response) vary across the parameter space; plotted against two variables at a time. (d) The variation of predicted values (obtained from regression of Equation (1)) as a function of experimental values reveals close correspondence between the model and experimental data (dashed line indicates y = x).

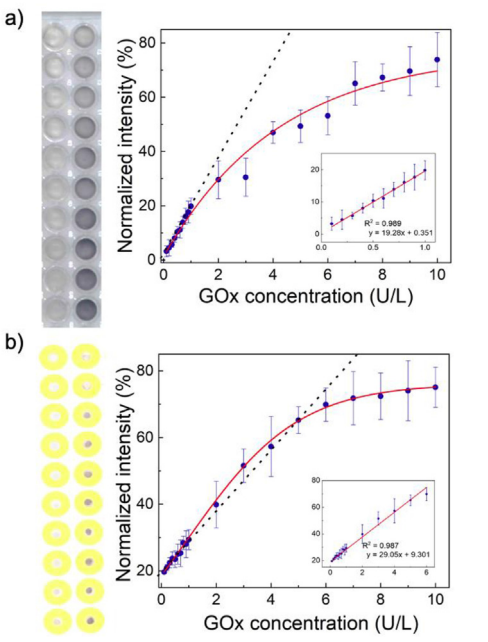

Fig. 3. A study of the colorimetric response due starch–iodide complexation in the presence of GOx and glucose under optimized conditions ($N = 3$). (a) Variation of intensity as a function of GOx concentration for experiments performed in microwell plate format. The photo (left) shows the assay solutions in the microwells, with GOx concentration increasing down the columns. (b) Variation of intensity as a function of GOx concentration for experiments performed in the PAD device. The photo (left) shows the paper device, with GOx concentration increasing down the columns. Insets show the linear response regions for both microwell- and paper-based assays, and the black dashed lines indicate the position of the linear range in the context of the whole data set.

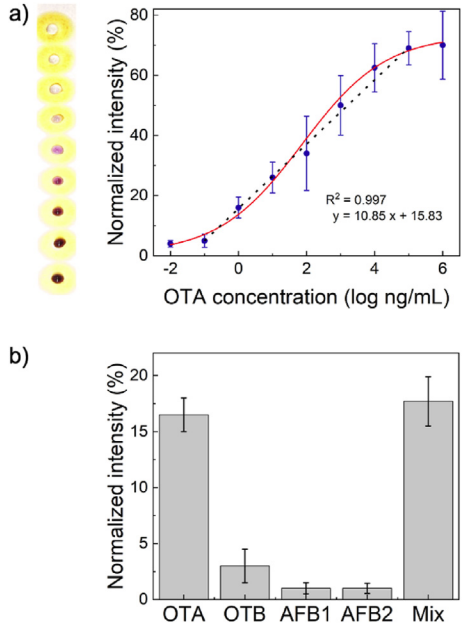

Fig. 4. Characterization of the paper-based assay. (a) A calibration curve presenting normalized signal intensity obtained from the corresponding PAD image as a function of OTA concentration, ($N = 5$). (b) Normalized signal intensity from the PADs in the presence of potential interferents (OTB, AFB1, and AFB2 at 10 ng mL^{-1}) and OTA at 1 ng mL^{-1}, and their mixture ($N = 3$).

analysis, as shown in Fig. 4a. Variation of extracted intensity values ($N = 5$) as a function of OTA concentration was linear between 10^{-1} and 10^{5} ng mL^{-1} (Fig. 4a dashed line), with an LOD and LOQ for OTA of 20 pg mL^{-1} and 320 pg mL^{-1}, respectively. Moreover, comparison

Table 3
A comparison of reported colorimetric detection techniques for OTA determination.

Year	Bio-recognition elements	LOD (ng mL^{-1})	Linear range (ng mL^{-1})	Sample	References
2014	Aptasensor and DNAzyme	0.4	N/A	Buffer	[38]
2016	CMOS sensor	2	2–10	Beer and Wine	[39]
2016	Aptasensor and Au@Fe_3O_4	0.03	0.5–100	Cereal	[40]
2017	Aptasensor and AuNPs	20	32–1024	White Wine	[41]
2018	ELISA with acid-base indicator	0.05	0.125–3.0	Corn	[42]
2018	ELISA/urease-induced AuNP	0.04	0.05–0.64	Corn, Rice, Wheat, White Wine	[43]
2018	Aptasensor/enzyme in liposome	0.023	0.05–2.0	Corn	[44]
2019	Aptasensor with nanozyme	0.35	0.5–120	Grape Juice	[45]
This work	Antibody/Aptasensor-GOx	0.025	0.1–10^5	Beer, Urine, and Human Serum	This work

of the LOD and linear range of the paper-based sensor with literature OTA colorimetric sensors (Table 3), confirms significant enhancements in sensor performance over the state-of-the-art.

Assay Selectivity: The selectivity of the biosensor was assessed by examination of its response to potential (and common) interferents, including ochratoxin B (OTB), aflatoxin B1 (AFB1), and aflatoxin B2 (AFB2). In all experiments, the concentration of each interferent was set to 10 ng mL^{-1}, a value that is an order of magnitude higher than OTA (1 ng mL^{-1}). Fig. 4b shows a high intensity signal for OTA, but a negligible response from all studied interferents, with signals originating from the pure OTA sample and mixed sample being identical. It should be noted that a marginally higher signal from OTB (versus AFB1 and AFB2) is expected since antiOTA exhibits trace binding with OTB (<1% in comparison with OTA, as indicated by the manufacturer) [34,35]. However, when compared to the pure OTA sample, such a signal is insignificant (*t*-value = 0.11, *t*-critical = 2.90, $N = 3$). Accordingly, the biosensor achieves excellent selectivity for OTA over OTB, AFB1, and AFB2, which is a direct result of the high selectivity inherent in the antibody-aptamer system.

Assay Accuracy: To validate the accuracy of the developed PAD system, we compared it to the gold standard method ultrahigh performance liquid chromatography (UPLC), and a previously developed electrochemical aptasensor [26]. Testing an OTA concentration series (1–10 ng mL^{-1}) with each method ($N = 3$), the PAD gave a coefficient of determination (R^2) of 0.985 against UPLC and 0.987 against the electrochemical aptasensor (Fig. 5a). A *t*-test comparison indicated no significant difference between each method, with excellent agreement at the 95% confidence level ($\alpha = 0.05$; *t*-values = 1.20 and 0.57 versus UPLC and the electrochemical aptasensor, respectively; *t*-critical = 2.30).

3.5. Complex sample analysis

Complex matrix validation was performed through the analysis of beer, artificial urine and human serum, all spiked to 1 ng mL^{-1} OTA. The results demonstrated excellent performance of the aptasensor in all matrices (Fig. 5b). The larger variance in serum was

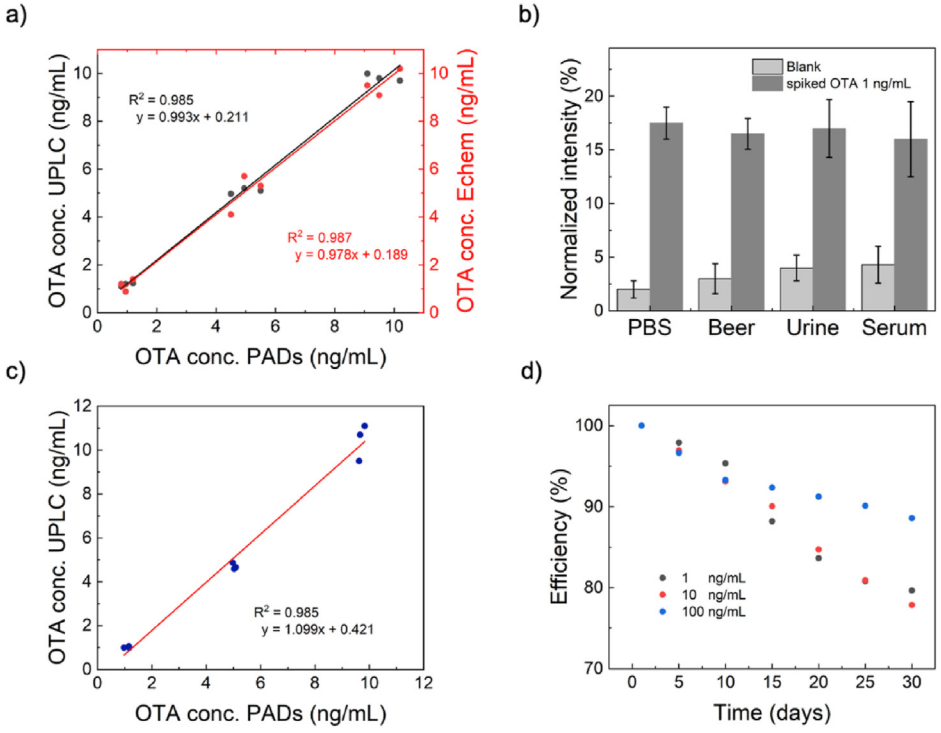

Fig. 5. Further characterization of the paper-based assay. (a) A comparison of OTA concentrations obtained when using the PAD, UPLC and an electrochemical aptasensor, to analyze standard solutions. (b) Normalized signal intensity obtained from the different sample matrices: PBS, beer, artificial urine and human serum, both blank and spiked with OTA to 1 ng mL^{-1}. (c) Comparison of OTA concentrations between the PADs and UPLC in beer samples spiked with OTA to 1, 5 and 10 ng mL^{-1}. (d) Variation of efficiency as a function of storage time for PADs detecting OTA (1, 10, and 100 ng mL^{-1}) over a period of 30 days ($N = 3$).

Table 4
Determination of OTA concentration in spiked beer samples comparing the PADs with UPLC, and comparing OTA concentration in blank and spiked artificial urine and human serum.

Sample	Spiked OTA	Detected (ng mL^{-1})		Recovery (%)		%RSD		t-value
	(ng mL^{-1})	PADs	UPLC	PADs	UPLC	PADs	UPLC	
Beer 1	1	0.98 ± 0.05	1.00 ± 0.02	98.00	99.69	4.99	2.63	0.07
	5	4.98 ± 0.20	4.86 ± 0.05	99.60	97.29	4.01	1.98	0.36
	10	9.63 ± 0.41	9.50 ± 0.32	96.30	94.97	4.32	1.01	0.3
Beer 2	1	1.17 ± 0.04	0.99 ± 0.04	117.0	99.17	3.39	0.46	0.15
	5	5.09 ± 0.12	4.66 ± 0.10	101.8	93.14	2.26	1.61	0.45
	10	9.83 ± 0.15	11.1 ± 0.31	98.30	110.71	1.49	0.55	0.33
Beer 3	1	1.16 ± 0.03	1.06 ± 0.05	116.0	105.8	2.58	1.41	0.46
	5	5.03 ± 0.25	4.59 ± 0.12	100.6	91.81	4.97	1.41	0.45
	10	9.66 ± 0.47	10.7 ± 0.35	96.60	107.5	4.93	0.7	0.41
Urine	1	0.96 ± 0.03	–	96.00	–	3.75	–	–
	5	5.08 ± 0.12	–	101.6	–	2.49	–	–
	10	10.0 ± 0.08	–	100.1	–	0.84	–	–
Human Serum	1	1.00 ± 0.03	–	100.0	–	3.76	–	–
	5	5.01 ± 0.07	–	100.2	–	1.55	–	–
	10	9.53 ± 0.25	–	95.30	–	2.69	–	–

likely due to the large amount of protein, predominantly serum albumin, interfering with sandwich complex formation [36]. Similarly, the artificial urine sample used in the current study contains 0.5% peptone, a soluble protein formed in the early stage of protein breakdown during digestion [37]. Thus, samples containing high concentrations of protein can slightly compromise detection efficiency through interference of the binding of AGOx and antiOTA with the analyte. Next, we spiked beer, artificial urine, and human serum with OTA at concentrations between 1 and 10 ng mL^{-1}, and calculated the detectable amount of OTA as a %recovery (Table 4). Significantly, all recoveries were measured to be between 95 and 117%, comparing well with corresponding recoveries from UPLC analyses. Further, we used the spiked beer samples as a direct comparison with UPLC (Fig. 5c), confirming excellent agreement between detection methods ($R^2 = 0.985$) with RSD less than 5%.

3.6. Assay stability

Reagents and device stability over extended periods of time are vital factors for the practical application of sensing systems. To assess shelf lifetimes, a set of PADs (totalling 500 detection chambers) was stored under nitrogen at 4 °C for up to 30 days. Color intensity (extracted using ImageJ) was then used to quantify the response for 1, 10, and 100 ng mL^{-1} OTA solutions in PBS (Fig. 5d). Collected data indicate a deterioration in response for all OTA concentrations when compared to data originating from freshly prepared PADs, however these were determined as not statistically significant (t-values for the three concentrations were 2.76, 3.26, and 4.18 for 1, 10, and 100 ng mL^{-1} ($N = 3$), respectively, with t-critical = 4.30). However, the average intensities originating from stored PADs did exhibit a 20% reduction in signal intensity (Fig. 5d), which is likely a result of partial denaturisation of the antibodies on the paper surface. Such effects could be further minimized by freeze-drying the PADs prior to storage.

4. Conclusions

We show for the first time the application of starch–iodide complexation as a colorimetric reagent in a PAD device for biomolecular detection using a sandwich-based assay format. Targeting OTA as a model analyte using an antibody–aptamer capture mechanism, we optimized reagent concentrations (iodine, starch, and glucose) using central composite design, and achieved an LOD of 20 pg mL^{-1}, an LOQ of 320 pg mL^{-1} and a linear range between 10^{-1} and 10^5 ng mL^{-1} (six orders of magnitude) against standard OTA solutions. The system exhibits excellent performance in complex matrices (human serum, artificial urine, and beer), comparing well with gold-standard UPLC. Overall, the sensing approach described herein exhibits great potential as a universal, environmentally friendly and cost-effective PAD biosensing platform to detect a wide range of analytes based on antibody and/or aptamer-based affinity reactions. We have demonstrated excellent sensitivity, selectivity, accuracy, precision and robustness in real-world samples, and excellent promise for universal point-of-use analyses. For example, this approach could be developed as an *in vitro* diagnostic device for widespread medical testing, and for deployment in resource-limited settings.

CRediT authorship contribution statement

Akkapol Suea-Ngam: Conceptualization, Methodology, Investigation, Formal analysis, Writing - original draft. **Leif-Thore Deck:** Investigation. **Philip D. Howes:** Methodology, Visualization, Supervision, Writing - review & editing. **Andrew J. deMello:** Methodology, Supervision, Project administration, Funding acquisition, Writing - review & editing.

Declaration of competing interest

The authors declare that they have no known competing financial interests or personal relationships that could have appeared to influence the work reported in this paper.

Acknowledgements

A. S. N would like to thank the State Secretariat for Education, Research and Innovation (SERI) in Switzerland for a Swiss Government Excellence Scholarship (ESKAS No. 2016.0728).

Appendix A. Supplementary data

Supplementary data to this article can be found online at

https://doi.org/10.1016/j.aca.2020.08.028.

References

[1] S. Harvey, On the detection of lead in potable waters by means of potassium bichromate, Analyst 6 (1881) 146–148.
[2] M. Jaffé, Ueber den Niederschlag, welchen Pikrinsäure in normalem Harn erzeugt und über eine neue Reaction des Kreatinins, Z. Physiol. Chem. 10 (1886) 391–400.
[3] E.R. Budden, H. Hardy, Preliminary notes on the colorimetric estimation of minute quantities of lead, copper, tin, and iron, Analyst 19 (1894) 169–178.
[4] A.W. Martinez, S.T. Phillips, M.J. Butte, G.M. Whitesides, Patterned paper as a platform for inexpensive, low-volume, portable bioassays, Angew. Chem. Int. Ed. 46 (2007) 1318–1320.
[5] A.W. Martinez, S.T. Phillips, G.M. Whitesides, Three-dimensional microfluidic devices fabricated in layered paper and tape, Proc. Natl. Acad. Sci. U.S.A. 105 (2008) 19606–19611.
[6] Y. Yang, E. Noviana, M.P. Nguyen, B.J. Geiss, D.S. Dandy, C.S. Henry, Based microfluidic devices: emerging themes and applications, Anal. Chem. 89 (2016) 71–91.
[7] W. Dungchai, O. Chailapakul, C.S. Henry, Electrochemical detection for paper-based microfluidics, Anal. Chem. 81 (2009) 5821–5826.
[8] M.M. Gong, D. Sinton, Turning the page: advancing paper-based microfluidics for broad diagnostic application, Chem. Rev. 117 (2017) 8447–8480.
[9] M.I.G. Almeida, B.M. Jayawardane, S.D. Kolev, I.D. McKelvie, Developments of microfluidic paper-based analytical devices (μPADs) for water analysis: a review, Talanta 177 (2018) 176–190.
[10] A. Mitchell, M. Mellon, Colorimetric determination of nickel with dimethylglyoxime, Ind. Eng. Chem., Anal. Ed. 17 (1945) 380–382.
[11] D. Quesada-González, A. Merkoçi, Nanomaterial-based devices for point-of-care diagnostic applications, Chem. Soc. Rev. 47 (2018) 4697–4709.
[12] S. Zeng, K.-T. Yong, I. Roy, X.-Q. Dinh, X. Yu, F. Luan, A review on functionalized gold nanoparticles for biosensing applications, Plasmonics 6 (2011) 491.
[13] P.D. Howes, S. Rana, M.M. Stevens, Plasmonic nanomaterials for biodiagnostic, Chem. Soc. Rev. 43 (2014) 3835–3853.
[14] N.A. Luechinger, E.K. Athanassiou, W.J. Stark, Graphene-stabilized copper nanoparticles as an air-stable substitute for silver and gold in low-cost ink-jet printable electronics, Nanotechnology 19 (2008) 445201.
[15] L.A.-W. Ellingsen, C.R. Hung, G. Majeau-Bettez, B. Singh, Z. Chen, M.S. Whittingham, A.H. Strømman, Nanotechnology for environmentally sustainable electromobility, Nat. Nanotechnol. 11 (2016) 1039.
[16] N. Khlebtsov, L. Dykman, Biodistribution and toxicity of engineered gold nanoparticles: a review of in vitro and in vivo studies, Chem. Soc. Rev. 40 (2011) 1647–1671.
[17] L. Bezinge, A. Suea-Ngam, A.J. deMello, C.-J. Shih, Nanomaterials for molecular signal amplification in electrochemical nucleic acid biosensing: recent advances and future prospects for point-of-care diagnostics, Mol. Syst. Des. Eng. 5 (2020) 49–66.
[18] X. Weng, G. Gaur, S. Neethirajan, Rapid detection of food allergens by microfluidics ELISA-based optical sensor, Biosensors 6 (2016) 24.
[19] S. Madhu, H.A. Evans, V.V. Doan-Nguyen, J.G. Labram, G. Wu, M.L. Chabinyc, R. Seshadri, F. Wudl, Infinite polyiodide chains in the pyrroloperylene–iodine complex: insights into the starch–iodine and perylene–iodine complexes, Angew. Chem. Int. Ed. 55 (2016) 8032–8035.
[20] R. McCready, J. Guggolz, V. Silviera, H. Owens, Determination of starch and amylose in vegetables, Anal. Chem. 22 (1950) 1156–1158.
[21] J. Nie, T. Brown, Y. Zhang, New two dimensional liquid-phase colorimetric assay based on old iodine–starch complexation for the naked-eye quantitative detection of analytes, Chem. Commun. 52 (2016) 7454–7457.
[22] Y. Liu, L. Lei, Z. Zhang, An ultrasensitive colorimetric immunoassay based on glucose oxidase catalyzed cascade formation of blue–black iodine–starch complex, Sens. Actuators, B 248 (2017) 195–200.
[23] M.-M. Liu, X. Lian, H. Liu, Z.-Z. Guo, H.-H. Huang, Y. Lei, H.-P. Peng, W. Chen, X.-H. Lin, A.-L. Liu, A colorimetric assay for sensitive detection of hydrogen peroxide and glucose in microfluidic paper-based analytical devices integrated with starch-iodide-gelatin system, Talanta 200 (2019) 511–517.
[24] F. Malir, V. Ostry, A. Pfohl-Leszkowicz, J. Malir, J. Toman, Ochratoxin A: 50 years of research, Toxins 8 (2016) 191.
[25] Y. Peng, V. Van Gelder, A. Amaladoss, K.H. Patel, Covalent binding of antibodies to cellulose paper discs and their applications in naked-eye colorimetric immunoassays, JoVE 116 (2016), e54111.
[26] A. Suea-Ngam, P.D. Howes, C. Stanley, A.J. deMello, An exonuclease I-assisted silver-metallized electrochemical aptasensor for ochratoxin A detection, ACS Sens. 4 (2019) 1560–1568.
[27] A. Suea-Ngam, P. Rattanarat, K. Wongravee, O. Chailapakul, M. Srisa-Art, Droplet-based glucosamine sensor using gold nanoparticles and polyaniline-modified electrode, Talanta 158 (2016) 134–141.
[28] D. Wei, X. Wu, J. Xu, F. Dong, X. Liu, Y. Zheng, M. Ji, Determination of Ochratoxin A contamination in grapes, processed grape products and animal-derived products using ultra-performance liquid chromatography-tandem mass spectroscopy system, Sci. Rep. 8 (2018) 2051.
[29] J.M. Gardner, M. Abrahamsson, B.H. Farnum, G.J. Meyer, Visible light generation of iodine atoms and I– I bonds: sensitized I– oxidation and I3– photodissociation, J. Am. Chem. Soc. 131 (2009) 16206–16214.
[30] Z. Wang, B. Chen, X. Zhang, Y. Li, W. Fang, X. Yu, L. Dang, Fractionation of kudzu amylose and amylopectin and their microstructure and physicochemical properties, Starch Staerke 69 (2017) 1500305.
[31] M.A. Bezerra, R.E. Santelli, E.P. Oliveira, L.S. Villar, L.A. Escaleira, Response surface methodology (RSM) as a tool for optimization in analytical chemistry, Talanta 76 (2008) 965–977.
[32] A. Suea-Ngam, M. Srisa-Art, Y. Furutani, PDMS-based microfluidic device for infrared-transmission spectro-electrochemistry, Bull. Chem. Soc. Jpn. 91 (2018) 728–734.
[33] A. Suea-Ngam, P.D. Howes, M. Srisa-Art, A.J. DeMello, Droplet microfluidics: from proof-of-concept to real-world utility? Chem. Commun. 55 (2019) 9895–9903.
[34] L. Bonel, J.C. Vidal, P. Duato, J.R. Castillo, Ochratoxin A nanostructured electrochemical immunosensors based on polyclonal antibodies and gold nanoparticles coupled to the antigen, Anal. Meth. 2 (2010) 335–341.
[35] Bio-Rad Datasheet, Rabbit Anti Aspergillus Ochraceus Ochratoxin A, 2020, 6999-2130.
[36] G. Fanali, A. Di Masi, V. Trezza, M. Marino, M. Fasano, P. Ascenzi, Human serum albumin: from bench to bedside, Mol. Aspect. Med. 33 (2012) 209–290.
[37] T. Brooks, C. Keevil, A simple artificial urine for the growth of urinary pathogens, Lett. Appl. Microbiol. 24 (1997) 203–206.
[38] J. Lee, C.H. Jeon, S.J. Ahn, T.H. Ha, Highly stable colorimetric aptamer sensors for detection of ochratoxin A through optimizing the sequence with the covalent conjugation of hemin, Analyst 139 (2014) 1622–1627.
[39] D. Bueno, L. Valdez, J. Gutiérrez Salgado, J. Marty, R. Muñoz, Colorimetric analysis of ochratoxin a in beverage samples, Sensors 16 (2016) 1888.
[40] C. Wang, J. Qian, K. Wang, X. Yang, Q. Liu, N. Hao, C. Wang, X. Dong, X. Huang, Colorimetric aptasensing of ochratoxin A using Au@ Fe3O4 nanoparticles as signal indicator and magnetic separator, Biosens. Bioelectron. 77 (2016) 1183–1191.
[41] X. Yin, S. Wang, X. Liu, C. He, Y. Tang, Q. Li, J. Liu, H. Su, T. Tan, Y. Dong, Aptamer-based colorimetric biosensing of ochratoxin A in fortified white grape wine sample using unmodified gold nanoparticles, Anal. Sci. 33 (2017) 659–664.
[42] K. Pei, Y. Xiong, X. Li, H. Jiang, Y. Xiong, Colorimetric ELISA with an acid–base indicator for sensitive detection of ochratoxin A in corn samples, Anal. Meth. 10 (2018) 30–36.
[43] K. Pei, Y. Xiong, B. Xu, K. Wu, X. Li, H. Jiang, Y. Xiong, Colorimetric ELISA for ochratoxin A detection based on the urease-induced metallization of gold nanoflowers, Sens. Actuators, B 262 (2018) 102–109.
[44] C. Lin, H. Zheng, M. Sun, Y. Guo, F. Luo, L. Guo, B. Qiu, Z. Lin, G. Chen, Highly sensitive colorimetric aptasensor for ochratoxin A detection based on enzyme-encapsulated liposome, Anal. Chim. Acta 1002 (2018) 90–96.
[45] F. Tian, J. Zhou, B. Jiao, Y. He, A nanozyme-based cascade colorimetric aptasensor for amplified detection of ochratoxin A, Nanoscale 11 (2019) 9547–9555.